Book Chapter

Effect of Copper Addition on the AlCoCrFeNi High Entropy Alloys Properties via the Electroless Plating and Powder Metallurgy Technique

Mohamed Ali Hassan[1], Hossam M Yehia[2], Ahmed SA Mohamed[1,3], Ahmed Essa El-Nikhaily[4] and Omayma A Elkady[5]*

[1]Mechanical Department, Faculty of Technology and Education, Sohag University, Egypt
[2]Mechanical Department, Faculty of Technology and Education, Helwan University, Egypt
[3]High Institute for Engineering and Technology, Egypt
[4]Mechanical Department, Faculty of Technology and Education, Suez University, Egypt
[5]Powder Technology Department, Central Metallurgical R & D Institute, Egypt

***Corresponding Author:** Omayma A Elkady, Powder Technology Department, Central Metallurgical R & D Institute, P.O. Box 87 Helwan, Cairo 11421, Egypt

Published **August 11, 2021**

This Book Chapter is a republication of an article published by Omayma A Elkady, et al. at Crystals in May 2021. (Hassan, M.A.; Yehia, H.M.; Mohamed, A.S.A.; El-Nikhaily, A.E.; Elkady, O.A. Effect of Copper Addition on the AlCoCrFeNi High Entropy Alloys Properties via the Electroless Plating and Powder Metallurgy Technique. Crystals 2021, 11, 540. https://doi.org/10.3390/cryst11050540)

How to cite this book chapter: Mohamed Ali Hassan, Hossam M Yehia, Ahmed SA Mohamed, Ahmed Essa El-Nikhaily, Omayma A Elkady. Effect of Copper Addition on the AlCoCrFeNi High Entropy Alloys Properties via the Electroless

Plating and Powder Metallurgy Technique. In: M Iqbal Khan, editor. Prime Archives in Material Science: 3rd Edition. Hyderabad, India: Vide Leaf. 2021.

Author Contributions: Mohamed Ali Hassan.: Conceptualization, data analysis, writing original draft and preparation, Hossam M. Yehia.: Investigate, writing original draft, review and editing, A.S.A. Mohamed.: review and editing, Ahmed Essa El-Nikhaily: Investigation and review, Omayma A. Elkady.: Methodology, review and editing. All authors have read and agreed to the published version of the manuscript.

Funding: This research received no external funding

Conflicts of Interest: The authors declare no conflict of interest.

Abstract

To improve the AlCoCrFeNi high entropy alloys' (HEAs') toughness, it was coated with different amounts of Cu then fabricated by the powder metallurgy technique. Mechanical alloying of equiatomic AlCoCrFeNi HEAs for 25 h preceded the coating process. The established powder samples were sintered at different temperatures in a vacuum furnace. The HEAs samples sintered at 950˚C exhibit the highest relative density. The AlCoCrFeNi HEAs model sample was not successfully produced by the applied method due to the low melting point of aluminum. The Al element's problem disappeared due to encapsulating it with a copper layer during the coating process. Because the atomic radius of the copper metal (0.1278 nm) is less than the atomic radius of the aluminum metal (0.1431 nm) and nearly equal to the rest of the other elements (Co, Cr, Fe, and Ni), the crystal size powder and fabricated samples

decreased by increasing the content of the Cu wt%. On the other hand, the lattice strain increased. The microstructure revealed that the complete diffusion between the different elements to form high entropy alloy material was not achieved. A dramatic decrease in the produced samples' hardness was observed where it decreased from 403 HV at 5 wt% Cu to 191 HV at 20 wt%Cu. On the contrary, the compressive strength increased from 400.034 MPa at 5 wt% Cu to 599.527 MPa at 15 wt% Cu with a 49.86% increment. This increment in the compressive strength may be due to precipitating the copper metal on the particles' surface in the nano-size, reducing the dislocations' motion, increasing the stiffness of produced materials. The formability and toughness of the fabricated materials improved by increasing the copper's content. The thermal expansion has increased gradually by increasing the Cu wt%.

Keywords

High Entropy Alloys; Electroless Copper Plating; Thermal Expansion; Hardness; Compressive Strength

Introduction

The high entropy alloys (HEAs) are a novel class of materials that are different from conventional alloys, which contains only one or two base elements. HEAs usually consist of more than four main elements. It has already been coined because the entropy is substantially higher under two conditions. One is when there are more significant elements in the mix, and the other is when their proportions are nearly equal. HEAs are characterized by high strength and hardness, high thermal stability, and excellent corrosion resistance. However, it suffers from high brittleness [1–9]. The lattice crystal structures of most HEAs are either body-centered cubic (BCC) [10] or face-centered cubic (FCC) [11]. HEAs with BCC structure exhibit low plasticity yet high strength, while FCC-structured HEAs have increased mobility with low strength [12]. The choice of elements for HEAs' design is essential when taking the specific applications and economical alloy into consideration [13,14]. A variety of alloys focusing on the influence of different elements

on HEAs, such as Al [15], Ni [16], Cu [17], Ti [18], and Sn [19], have been widely published.

Recently, many HEA systems have been exploited, and most research focused on the microstructure and properties of the Al*x*CoCrFeNi HEAs system [20–22]. The addition of copper (Cu) to a HEA matrix has been widely investigated [23]; this is probably because the atomic radii of elements are close to one another and because there is a tendency to form a reliable solution according to the phase rule and phase diagram between them [24]. The main difference between AlxCoCrFeNi and AlCoCrFeNiCux is the presence of the Cu-rich phases at last. This is because Cu has positive enthalpy mixtures with most other elements and has thus repelled to the inter-dendrite (IR) region [25]. Moreover, the remnant Cu in the dendritic area also clusters and forms various sediments [26]. The investigators also found that the Cu element can enhance the FCC phase formation [27]. Furthermore, the increase in copper content decreases the oxidation ratio for AlCoCrCuxFeNi HEAs [28].

The AlCoCrFeNiCu is preferentially produced via conventional metallurgy, for example, arc melting or induction melting [29]. These methods result predominantly in a dendritic microstructure. Additionally, high interfacial energy between the molten metals and Cu reinforcement particles reduces the wettability, which causes the formation of pores that profoundly affect electrical conductivity. Consequently, it renders the casting technique applications for the copper matrix composites [30]. Furthermore, the machining needed for the final parts could be challenging due to these alloys' high hardness. Therefore, powder metallurgy (PM) could be a suitable alternative technique for the manufacturing process. The process has been described in the literature, where it is performed in three main steps: mixing, cold forming, and then sintering at a suitable temperature [31–34]. The PM process is characterized by no need for further machining, minimized scrap loss of raw materials, and facilitated alloying elements. To establish good adhesion and distribution for the copper element with the different alloying elements of the HEAs, and consequently, achieving high strength, the electroless precipitation process is

recommended. Additionally, this technique was suitable for the production of nano-sized copper metal, which improves the strength of material according to the Hall–Petch equation [35,36].

Hence, the purpose of the current study was to investigate the effect of sintering temperatures on the density, microstructure, physical, and mechanical properties of the $Cu_x/(AlCoCrFeNi)_{1-x}$ (x = 5, 10, 15, and 20 wt.%) fabricated by the powder metallurgy (PM) technique. Three various sintering temperatures were considered for all the prepared samples, 900, 950, and 1000 °C, to optimize the suitable sintering temperature for the preparation of $Cu_x/(AlCoCrFeNi)_{1-x}$ HEA.

Experimental Procedure

Material

In the present study, elemental powders with high purity (>99.5%) of Al, Cr, Co, Ni, and Fe with an average particle size (< 45 µm) supplied from Nore industrial and laboratory chemicals (Nilcco) - Cairo- Egypt were used as the start materials. The electroless plating of copper on the AlCoCrFeNi alloy powder particles was performed using a bath containing copper (II) sulfate pentahydrate, sodium hydroxide, potassium sodium tartrate, and formaldehyde. All chemicals were supplied by El- Alsharq Al'awsat Company for chemicals - Cairo- Egypt.

HEA Preparation

Al, Co, Cr, Ni, and Fe with an equimolar ratio were mixed in a stainless-steel container for 25 h using a stainless-steel balls with a 10-mm diameter at 120 rpm rotational speed. The process proceeded under argon atmosphere to avoid any oxidation. The ball to powder ratio (BPR) was 5:1. The mixing process was followed by the electroless copper coating from the bath, as shown in Table 1, to prepare four powder samples $Al_{19}Co_{19}Cr_{19}Fe_{19}Ni_{19}Cu_5$, $Al_{18}Co_{18}Cr_{18}Fe_{18}Ni_{18}Cu_{10}$, $Al_{17}Co_{17}Cr_{17}Fe_{17}Ni_{17}Cu_{15}$, and $Al_{16}Co_{16}Cr_{16}Fe_{16}Ni_{16}Cu_{20}$ of high entropy alloys. The coating process was established by dissolving copper sulfate, adjusting the pH ~12 by sodium

hydroxide, and adding Al20Co20Cr20Ni20Fe20 mixed powders. Finally, formaldehyde as a reducing agent was added to start the reaction. The coated HEAs powder samples were filtered, then dried in an electric furnace at 90 ^{o}C for 1 h. After the coating process was completed, the AlCoCrFeNi/Cu powders were filtered and washed with distilled water, and dried in an electric furnace at 90 °C for 2 h. The weight percentage of Cu was adjusted by weighing each powder sample after the coating process.

The nano copper was precipitated in cuprous oxide (CuO) due to Cu's oxidation during the electroless deposition process. Accordingly, in order to reduce CuO to pure Cu metal, the prepared HEAs powders were heated at 450 °C for 1 h under hydrogen atmosphere.

Cold compaction at 800 MPa using a universal hydraulic press was applied to consolidate the prepared Cu_x / $(AlCoCrFeNi)_{1-x}$ powder samples. All the obtained green materials were sintered in a vacuum furnace at different heating temperatures of 900, 950, and 1000 °C for 90 min by the heating cycle shown in Figure 1. Three holding temperatures during the sintering process were used. The first was the de-waxing step at 250 °C to remove paraffin wax, the second was at 850 °C to achieve high diffusivity for cobalt and other elements, and the last one was at 950 °C to complete the sintering process. Figure 2 illustrates the procedures of the preparation and fabrication of $(AlCoCrFeNi)_{1-x}$ /Cu_x HEAs materials.

Table 1: Electroless chemical composition bath of copper precipitation.

Materials	**Weight**
Copper (II) sulfate, ($CuSO_4$)	70 g/L
Potassium sodium tartrate, ($KNaC_4H_4O_6.5H_2O$)	170 g/L
Sodium hydroxide, (NaOH)	50 g/L
Formaldehyde	200 mL/L
Temperature	60 °C

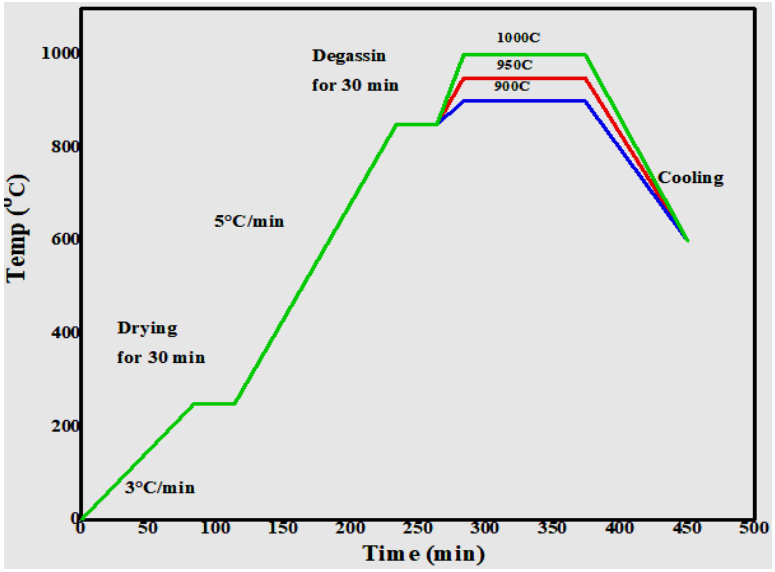

Figure 1: Heating cycle of the sintering process.

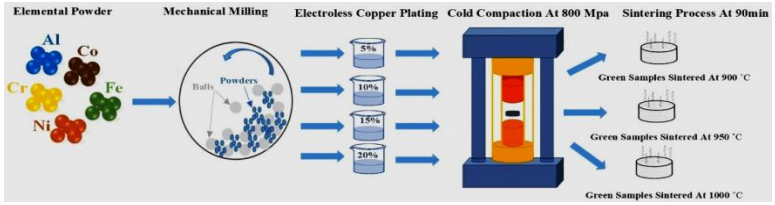

Figure 2: Flowchart of Cu_x /$(AlCoCrFeNi)_{1-x}$ HEAs powder samples' preparation and fabrication.

Characterization and Analysis

The bulk density of the sintered alloys was measured using Archimedes' rule according to the standard (ASTM B962-14) [37]. The sintered samples were weighed at room temperature in air and in distilled water as floating liquid.

$$\rho_{Arch} = \frac{W_{air}}{W_{air} - W_{water}} \quad (1)$$

The relative density (R_d) was determined using the following equation:

$$R_d = \frac{\rho_{Arch}}{\rho_{th}} \rho_{liquid} \quad (2)$$

where ρ_{Arch} is the Archimedes density, $\rho_{th.}$ is the theoretical density, and ρ_{liquid} is the liquid density.

The theoretical density ρ_{th} of the samples was calculated by using the following equation:

$$\rho_{\text{theo}} = \rho_{Cu} wt.\%_{Cu} + \rho_{Al} wt.\%_{Al} + \rho_{Co} wt.\%_{Co} + \rho_{Cr} wt.\%_{Cr} + \rho_{Fe} wt.\%_{Fe} + \rho_{Ni} wt.\%_{Ni} \quad (3)$$

where (ρ_{Cu}) and (wt.$\%_{\mathbf{Cu}}$) are the density and the weight percent of the Cu element, (ρ_{Al}) and (wt.$\%_{\mathbf{Al}}$) are the density and the weight percent of the Al element, (ρ_{Co}) and (wt.$\%_{\mathbf{Co}}$) are the density and the weight percent of the Co element, and (ρ_{Cr}) and (wt.$\%_{\mathbf{Cr}}$) are the density and weight percent of the Cr element, respectively.

In order to ensure the repeatability of the test, we recommend performing it for three times as a range. For microstructure observation, sample surfaces were prepared using silicon carbide papers (SiC) with 600, 800, 1000, and 1200 grades, respectively.

The crystal and phase structure of the powder and consolidated samples were investigated using (X'pert PRO PANalytical) a PANalytical X'Pert Pro device (Panalytical, Almelo, The Netherlands) X-ray diffraction with Cu kα radiation (λ=0.15406 nm). The 0.02° scan rate in a range of 20° to 100° was used. The Scherrer equation [38] was used to calculate the crystallite size of the coated powders using the XRD peak broadening equation as follows:

$$D = \frac{0.9\lambda}{B\cos\theta} \quad (4)$$

While the lattice strain ε was determined based on Equation (5) introduced by Danilchenko et al. [39] as follows:

$$\varepsilon = \frac{B}{4tan\theta} \quad (5)$$

where D is the crystallite size, B is the full width at half maximum (FWHM), λ is the wavelength, and θ is the peak position.

Scanning electron microscopy (SEM, FEI model 'Philips XL30′) FE-SEM (Philips XL 30, Royal Dutch Philips Electronics Ltd., Amsterdam, Nederland) equipped with back scattered-electron (BSE) mode and an energy dispersive X-ray spectroscopy (EDX) microanalysis system (operated at accelerating voltage 20 kV, 1.2 nA beam current, and 10 microsecond dwell time for minimizing SEM image noise) was used to characterize the morphology and microregion composition of sintered samples.

The Vickers hardness (micro and macro-hardness) of fabricated HEAs alloys using a Leitz Durimet microhardness tester (Leitz, Oberkochen, Germany) and Vickers hardness tester model 5030 SKV England (Indentec **5030 SKV**,. Stourbridge, West Midlands, **UK**) was measured. The micro-hardness test was performed by a Vickers indenter under a static load of 25 g and a dwell time of 5 s according to the (ASTM E384-11) at the temperature of 25°C ± 3°C [40]. On the other hand, Vicker's macro hardness was measured at 10 kg for 15 s. The average of five readings for each hardness value was calculated. A digital indicator with 0.001-mm precision and an electrical furnace were used to investigate the thermal strain of the $Cu_x/(AlCoCrFeNi)_{1-x}$ alloys, and consequently, the coefficient of thermal expansion (CTE). The 3 °C/min heating and cooling rates in an argon atmosphere were used. The measurements of the thermal expansion were performed in the range of 100 to 350°C and repeated for three times.

The compressive strength test of the samples was measured using a uniaxial SHIMADZU universal testing machine (Shimatzu, Kyoto, Japan) (UH-F500KN). The ratio between the length and width of the used samples was 1. The applied cross-head speed of the used universal test machine was 3 mm/min. The test was performed at room temperature (25°C).

Results and Discussion

Density Measurement

The effect of the Cu proportion on the relative density of the Cux/(AlCoCrFeNi)1-x alloys at 900, 950, and 1000 ℃ are shown in Figure 3. In general, the sintered samples' relative density increased at all sintering temperatures by increasing the Cu ratio. Results revealed that 950 ℃ is the best suitable sintering temperature for achieving the $Cu_x/(AlCoCrFeNi)_{1-x}$ HEAs' highest densification. Experimentally, the AlCoCrFeNi alloy was not established in these sintering conditions, which is why its density was excluded from the present results. The addition of copper to the AlCoCrFeNi HEA facilitates the sintering process and a 98% relative density at $Al_{16}Co_{16}Cr_{16}Fe_{16}Ni_{16}\mathbf{Cu_{20}}$ was achieved. Copper precipitated in the nano size, which helps to reduce the heating temperature of sintering. Additionally, its presence on the grain boundaries of the AlCoCrFeNi facilitates the interfacial bonding and then impedes the formation of micropores or voids during the sintering process. On the other hand, the electroless process' reduction in crystallite size helped increase the surface area, which enhances the diffusion phenomenon. Accordingly, the relative density gets closer to the theoretical one [41,42]. Sintering at 900 ℃ records the lowest densification for the prepared samples. This reduction in densification may be due to the particles' low diffusion temperature of the different elements. So, little densification takes place and, consequently, low density is achieved. On the other hand, the reduction in density values at 1000 ℃ may be due to copper swelling during the sintering process [43].

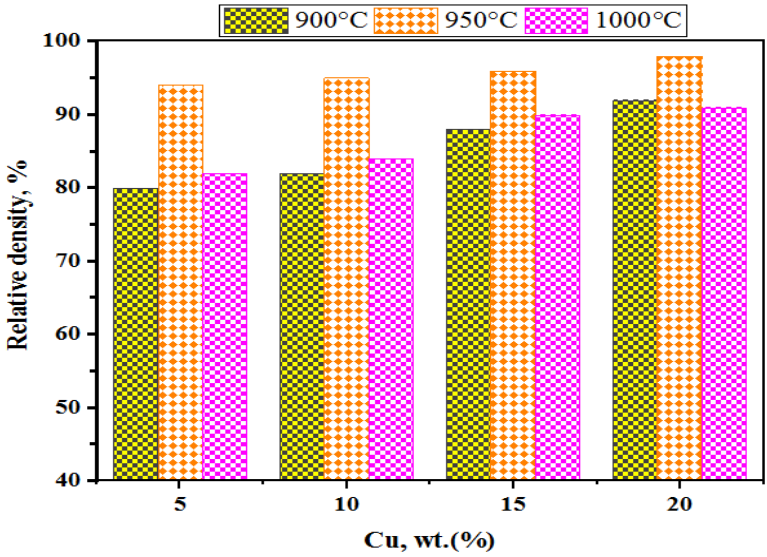

Figure 3: Relative density for Cu_x/ $(AlCoCrFeNi)_{1-x}$ HEAs sintered at 900, 950, and 1000 °C.

Microstructure Investigation

The prepared Cu_x / $(AlCoCrFeNi)_{1-x}$ alloy powders were characterized by FE-SEM (BSE), as shown in Figure 4**.** High homogeneity between all the constituents of the differently prepared powder alloys was observed. As a result of milling AlCoCrFeNi equiatomic HEAs for 25 h, cold welding between the powders occurred, and a flake powder shape was noted. Such preliminaries combined leads one to predict the formation of alloying between the used elements that will in turn form solid solution and consequently, the high entropy. Additionally, the reduction in the particle sizes facilitates the accumulation between the powders. The microstructure also shows a good coating of the nano-copper particle on AlCoCrFeNi particles' surface due to the high quality of the electroless Cu deposition process. An image for the precipitated nano copper after reduction by hydrogen is shown in the last picture to confirm its nano size.

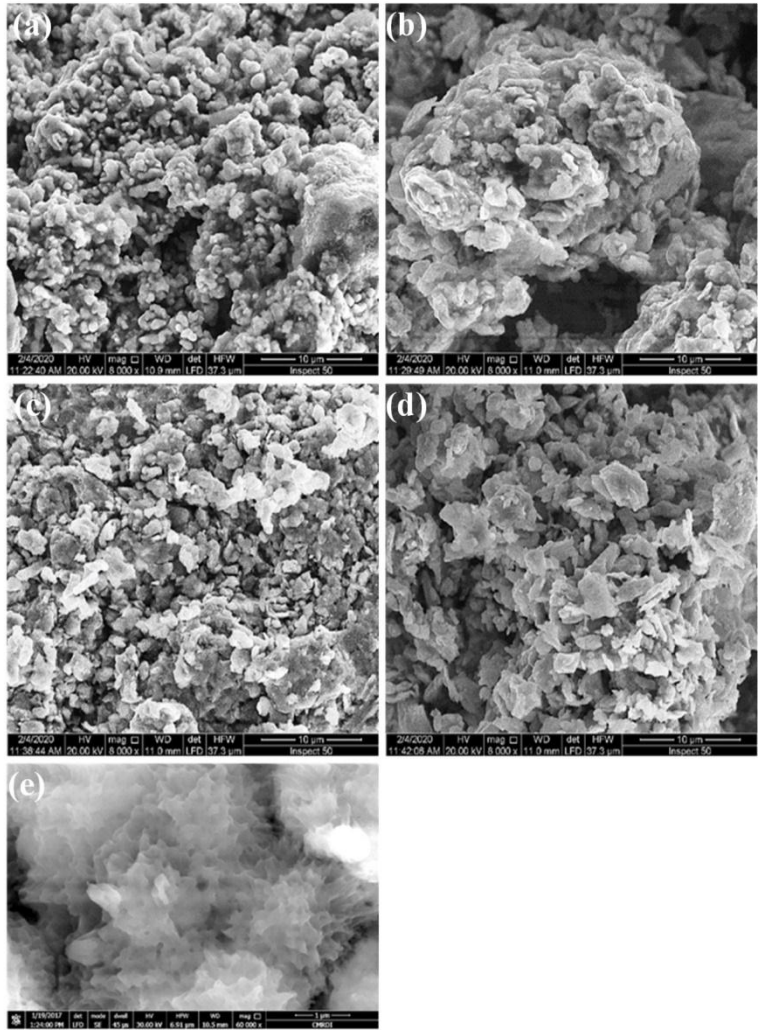

Figure 4: SEM (BSE) micrographs of the fabricated (a) $Al_{19}Co_{19}Cr_{19}Fe_{19}Ni_{19}Cu_5$, (b) $Al_{18}Co_{18}Cr_{18}Fe_{18}Ni_{18}Cu_{10}$, (c) $Al_{17}Co_{17}Cr_{17}Fe_{17}Ni_{17}Cu_{15}$, (d) $Al_{16}Co_{16}Cr_{16}Fe_{16}Ni_{16}Cu_{20}$ and (e) Pure precipitated Cu powder alloys.

The mapping analysis of the 20 wt% Cux/ (AlCoCrFeNi) 1-x powder alloy is shown in Figure 5**.** The mapping illustrates a high homogeneous distribution of the prepared element powder alloys. It confirmed the presence of all the used raw materials.

No oxides were detected, which means an excellent mixing control atmosphere and a reasonable reduction of CuO.

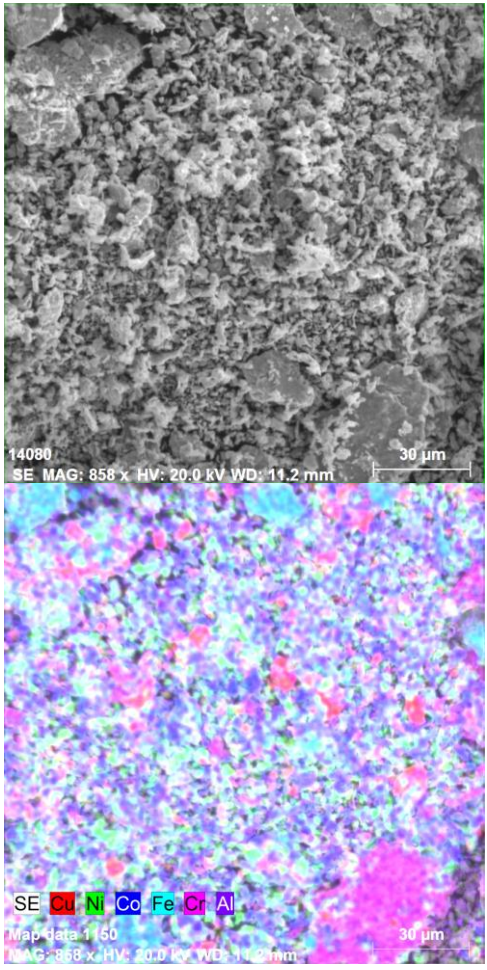

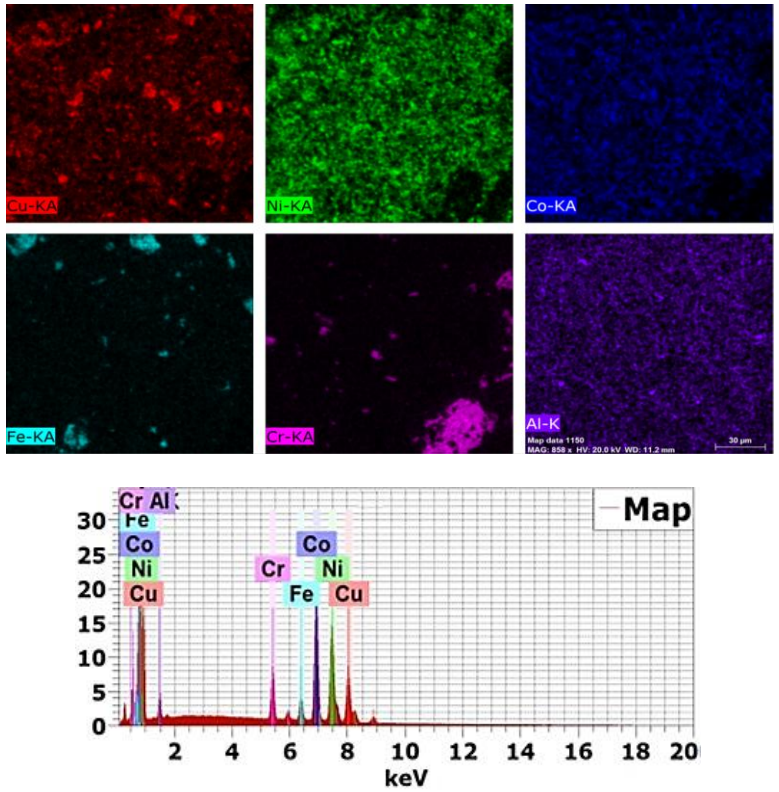

Figure 5: Mapping of the $Al_{16}Co_{16}Cr_{16}Fe_{16}Ni_{16}\mathbf{Cu_{20}}$ powder sample.

Figure 6 illustrates the Cu content's effect on the microstructure of the AlCoCrFeNi HEAs fabricated at 950 °C. The microstructures of the sintered samples **a, b, c,** and **d** show a homogeneous distribution of all the constituent elements that are well-bonded and connected. Three distinct regions are observed from the microstructure: the first is the dark area, which is believed to be the Cr-rich BCC; the second is the bright one, which refers to the Cu rich FCC; and the third is the AlCoCrFeNi matrix FCC. Agglomerations of Cr appeared due to the milling process. As shown, Al, Co, Fe, and Ni entirely merged with each other, and an FCC solid solution formed. The solid solution formed in the principal return of the prior mechanical milling and establishes the alloying process between the different elements. On the other hand, the Cu and Cr elements did not dissolve to participate in the formation of high

entropy alloys. Based on this result of the microstructure, the completion of high entropy alloys formation was not achieved with the powder metallurgy technique under the current conditions. As the Cu element increases, the dominant phases of the Cu_x/ $(AlCoCrFeNi)_{1-x}$ alloy switches to the FCC (matrix, Cu rich) phase, and the amount of the Cr-rich BCC phase decreases. Cr versus Cu's reduction resulting from negative vacancy-formation energies indicates a thermodynamic drive for Cr to segregate [44]. Coating AlCoCrFeNi HEA by copper reduces the surface energy between the surfaces of the elements and consequently improves the wettability, and excellent adhesion between all elements of the alloys is achieved. No pores were noticed, which means high densification for all fabricated alloys.

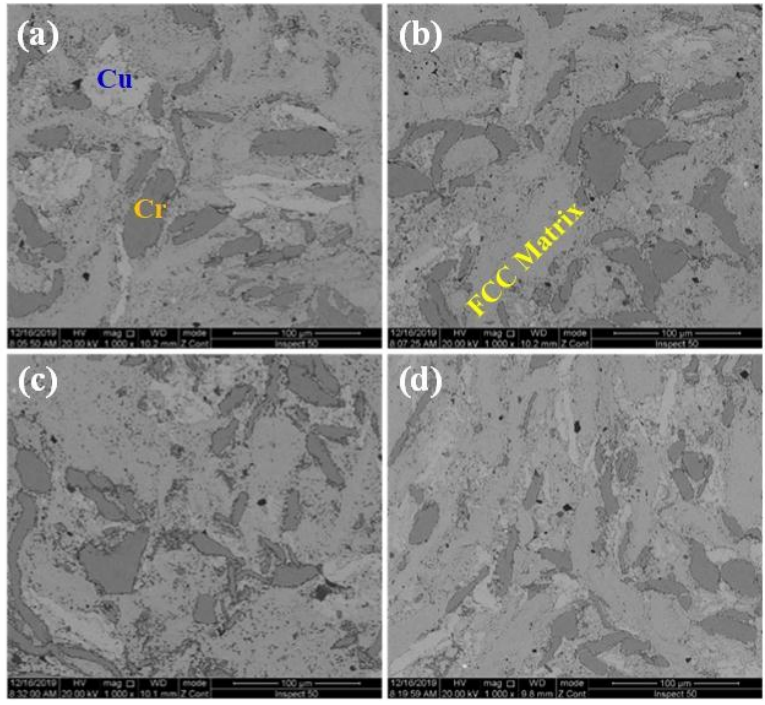

Figure 6: SEM-BSE micrographs of the fabricated (**a**)$Al_{19}Co_{19}Cr_{19}Fe_{19}Ni_{19}$**Cu$_5$**, (**b**)$Al_{18}Co_{18}Cr_{18}Fe_{18}Ni_{18}$**Cu$_{10}$**, (**c**)$Al_{17}Co_{17}Cr_{17}Fe_{17}Ni_{17}$**Cu$_{15}$**, and (**d**) $Al_{16}Co_{16}Cr_{16}Fe_{16}Ni_{16}$**Cu$_{20}$** samples.

The SEM-EDX elemental mapping of the four fabricated HEAs samples is shown in Figure 7**.** The mapping represents the distribution of each element in the formed piece with a different color. Six principal components, including Al (red), Co (rose), Cr (green), Cu (yellow), Fe (blue), and Ni (magenta), were observed. Clear agglomeration of the Cr element, which prevents the formation of the high entropy alloys, is evident in all samples. As shown, the Cu element tends to dissolve with the FCC phase that represents the matrix of all the fabricated pieces.

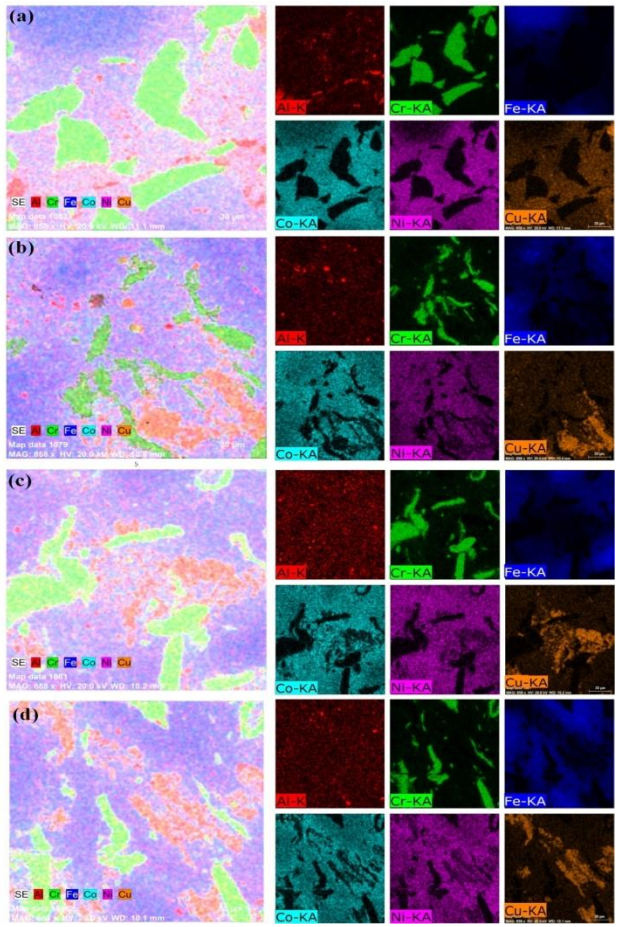

Figure 7: Mapping chart of the fabricated (a) $Al_{19}Co_{19}Cr_{19}Fe_{19}Ni_{19}Cu_5$, (b) $Al_{18}Co_{18}Cr_{18}Fe_{18}Ni_{18}Cu_{10}$, (c) $Al_{17}Co_{17}Cr_{17}Fe_{17}Ni_{17}Cu_{15}$, and (d) $Al_{16}Co_{16}Cr_{16}Fe_{16}Ni_{16}Cu_{20}$ samples at 950 °C.

XRD of the Powder and Sintered HEAs

The X-ray diffraction details of the Cu_x/ $(AlCoCrFeNi)_{1-x}$ HEA powders at room temperature are shown in Figure 8. The figure reflects the impact of the Cu content on the chemical composition and crystal structure of the AlCoCrFeNi. It was observed that the peak intensity of Cu became shinier by increasing its percentage. No new intermetallics were formed as a result of milling or electroless plating processes. The first peak of Al and Co completely disappeared, which is consistent with Shivam et al. [45]. Shivam et al. investigated the influence of milling times at 0, 5, 10, 15, 20, 25, and 30 h on the crystal structure and chemical composition of AlCoCrFeNi HEA powders. The results revealed that the first peak of Al dissipated at 10, which is attributed to the lower melting temperature of Al, indicating the possibility of dissolving in the host lattice of Fe/Cr. They observed that the Fe structure's solid solution is formed by increasing the milling time up to 20 h. Further milling proceeded up to 30 h to become more homogenized solid solution with more refined grains. Suryanarayana C et al. [46] revealed that forming a solid solution phase might mainly be attributed to the high entropy and stronger bonding among constituent elements, atomic size difference, and electro-negativities of the atoms.

As Shang et al. [47] investigated the effect of different milling times on CoCrFeNiW HEA powders' physical properties, they found that the used element's spectrum was still visible and evident up to 40 h. This study also demonstrated that the elements' peaks do not disappear simultaneously; for example, Cr and Fe's crystalline peaks go thoroughly after 40 h, while Co also dissolves after 5 h of milling. From those mentioned above, one can notice the elements dissolving and transforming into FCC or BCC phases. It is not related to a specific milling time and does not indicate the ideal milling conditions. Copper oxide phases (CuO and Cu_2O) were not found at the XRD spectrum, proving that the deposited copper has high purity with all molecule compositions in the electroless bath [48].

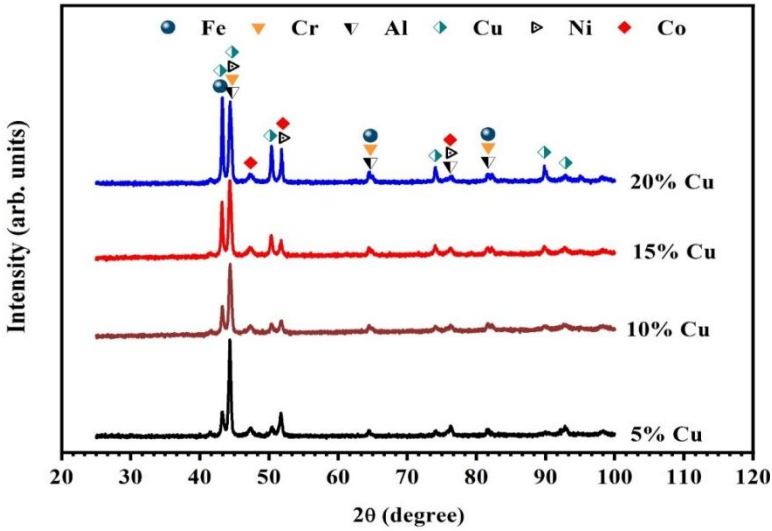

Figure 8: XRD patterns of the $Cu_x/(AlCoCrFeNi)_{1-x}$ powder alloys after milling and Cu coating**.**

The crystal size and lattice strain of the $Cu_x/ (AlCoCrFeNi)_{1-x}$ powder alloys were calculated from the X-ray peak broadening using Scherrer's formula and are presented in Table 2**.** The crystallite size was significantly refined as the weight percentage of the increased Cu. The refining in the particle size by increasing the Cu wt% was attributed to the precipitation of copper in nanoscale size. Coating the mixed Al, Co, Cr, Fe, and Ni with a layer of nano Cu particles prevents the green growth between the constituent particles. So, grain refining takes place. On the other hand, the lattice strain results revealed that the lattice string increases by increasing the Cu wt % deposited layer. Generally, the reasons for the increment in the lattice strain can be attributed to the size mismatch effect between the elements, increasing the grain boundary fraction, and high mechanical deformation [49].

Table 2: Crystal size and lattice strain of the HEAs powder samples.

Wt.% Cu	Crystal Size (nm)	Lattice Strain (%)	Full width at Half Maximum (FWHM)
5	29.78	0.081	0.32
10	23.17	0.104	0.411
15	22.26	0.109	0.428
20	21.98	0.111	0.434

The XRD patterns of the HEAs sintered samples are shown in Figure 9. The peaks' broadening, height, and number changed after the sintering process, where the detected peaks' extension became more comprehensive, and their intensities smaller. Some peaks disappeared during the sintering process. These changes may be attributed to two main factors, i.e., high lattice strain and refined crystal size. The formation of a solid solution phase may mainly have participated in the high entropy and stronger bonding among constituent elements, atomic size difference, and electro-negativities of the atoms [50]. The X-ray reflects three crystalline structures (Cu-rich FCC 1, Cr-rich BCC, and matrix FCC 2). The total number of phases in the prepared alloys is well below the maximum number of equilibrium phases allowed by the Gibbs phase principles [51]. As seen from the XRD patterns, the Cr fertile BCC phase intensity is much higher than that of both FCC phases. This may be attributed to Al and Cr's presence in equal or higher concentrations than the other elements that stabilize the BCC structure **[52].** The Cr fertile BCC phase's relative intensity decreased by increasing the Cu content, which suggests that the weight fraction of the FCC phase increases with Cu reinforcement against the BCC phase [53]. The relative intensity of both FCC phases becomes more durable and more reliable by increasing the Cu content up to 20%. This is because the presence of Cu with higher concentrations supports the formation of the FCC structure [54]. It is primarily due to the purpose of BCC or FCC lattice crystallography investigated by the average periodic table group number or average valence electron concentration (VEC). FCC phases are motivated to be more stable at higher values of VEC ($\geq$8) while BCC phases maintain stability at lower VEC ($\leq$6.87). The addition of aluminum particles reduces the VEC value [55]. Thus, the alloy system spontaneously promotes crystal structure

transition from FCC to BCC to minimize the lattice distortion energy.

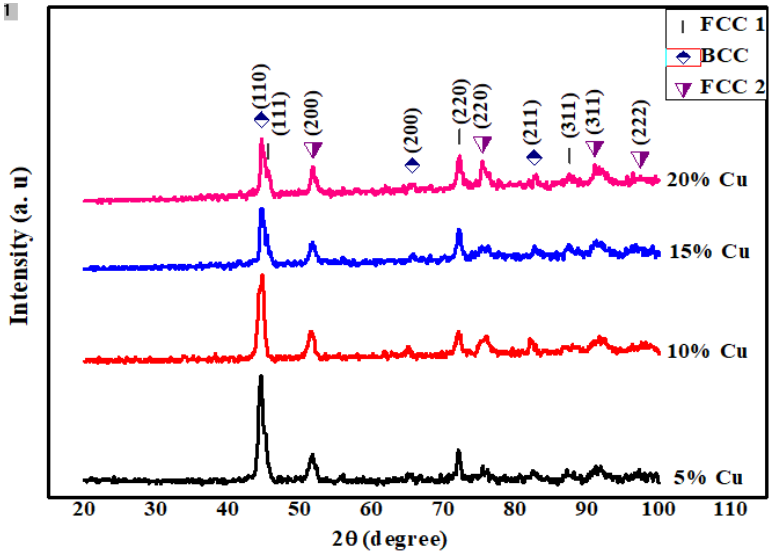

Figure 9: XRD patterns of the Cu_x/ $(AlCoCrFeNi)_{1-x}$ sintered at 950 °C.

The crystal size and lattice strain parameters of the fabricated Cu_x/ $(AlCoCrFeNi)_{1-x}$ alloys are arranged in Table 3. As shown in the **table**, the crystal size of fabricated HEAs decreased by increasing the precipitated Cu content, which is similar to the result of powder alloys. Additionally, the lattice strain increases by increasing the Cu content. The coating process of the milled AlCoCrFeNi probably affects the atoms' orders and, consequently, plans of the new material during the sintering process. So, the lattice strain distortion increased by increasing the content of the precipitated Cu layer on the surfaces of the AlCoCrFeNi HEA particles.

Table 3: Crystal size and lattice strain of the fabricated HEAs samples.

Wt.% Cu	Crystal Size (nm)	Lattice Strain (%)	Full width at Half Maximum (FWHM)
5	96.64	2.09	1.45
10	90.41	2.23	1.32
15	91.05	2.22	1.33
20	73.24	0.53	5.95

Figure 10 compares the crystallite sizes between the BCC and both FCC phases by the Scherrer formula. It is significantly noted that the crystallite size of the Cr fertile BCC phase was increased with an increase in the Cu electroless concentration. The crystallite sizes of both FCC phases were decreased with an increase in the Cu electroless concentration. This may be attributed to the increasing in the FCC weight fraction. The effect of Al addition on the BCC phase of the $Al_xCoCrCuFeNi$ HEAs using the Scherrer formula was investigated [56]. The calculations show that the increase in the Al content participates in increasing the BBC phase fraction and decreasing the crystallite size.

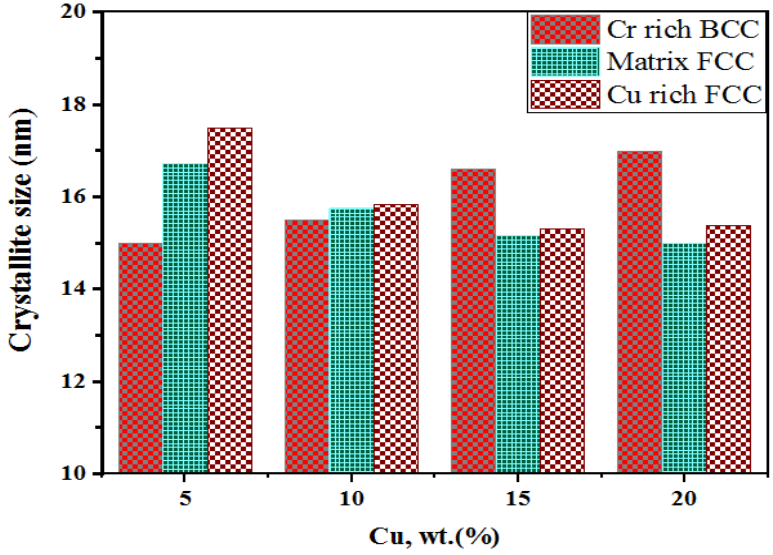

Figure 10: Crystallite sizes of the BCC and both FCC phases for the sintered samples.

Table 4 represents the chemical composition of the three phases obtained by SEM-EDX analysis of the fabricated Cux/ (AlCoCrFeNi)1-x HEAs samples. It was observed that the Al element has the lowest value in the chemical composition of all manufactured alloys. This may be attributed to the evaporation of Al at the sintering temperature, where it has the lowest melting temperature [30,57]. It also may be related to its high diffusivity in the FCC matrix. Moreover, apparently out of Table 4, both Al and Ni have the same content at Cr-rich BCC due to the segregation attributed to the different mixed enthalpy between Al, Ni, and Cr [58]. The melting point of elements and mixing enthalpy are two main influencing factors affecting the alloying rates [57]. In the solid state, the item with a low melting point has a higher intrinsic diffusion coefficient [59]. At lower temperatures (<300 °C), Cu and Cr are widely immiscible in the solid state and have large positive enthalpies of mixing [60,61].

Table 4: Chemical composition of the FCC and BCC phases obtained by SEM-EDX analysis from fabricated samples.

Alloy	Region	Mole fraction/at%					
		Al	**Co**	**Cr**	**Fe**	**Ni**	**Cu**
$Al_{19}Co_{19}Cr_{19}Fe_{19}Ni_{19}Cu_5$	Nominal	$(AlCoCrFeNi)_{95}$					5
	Cr rich BCC	0.55	3.65	88.93	2.12	3.03	1.71
	matrix FCC	5.01	30.12	14.41	5.74	26.31	18.40
	Cu rich FCC	1.46	10.13	5.80	2.60	15.52	64.49
$Al_{18}Co_{18}Cr_{18}Fe_{18}Ni_{18}Cu_{10}$	Nominal	$(AlCoCrFeNi)_{90}$					10
	Cr rich BCC	0.31	3.78	88.25	3.31	3.27	1.09
	matrix FCC	1.74	38.93	6.04	2.60	33.40	17.29
	Cu rich FCC	15.94	20.39	3.89	6.05	25.83	27.89
$Al_{17}Co_{17}Cr_{17}Fe_{17}Ni_{17}Cu_{15}$	Nominal	$(AlCoCrFeNi)_{85}$					15
	Cr rich BCC	0.04	3.40	87.89	3.39	2.91	2.37
	matrix FCC	1.51	20.42	21.45	23.59	16.90	16.14
	Cu rich FCC	0.85	10.13	5.60	5.72	12.01	65.68
$Al_{16}Co_{16}Cr_{16}Fe_{16}Ni_{16}Cu_{20}$	Nominal	$(AlCoCrFeNi)_{80}$					20
	Cr rich BCC	0.14	3.71	87.45	3.88	2.42	2.39
	matrix FCC	2.90	21.87	9.63	33.77	16.99	14.84
	Cu rich FCC	0.93	6.30	4.67	6.03	9.47	72.60

Hardness

Figure 11 illustrates the copper content effect on the micro and macro-hardness of the (AlCoCrFeNi) HEA sintered at 950 °C. Although improving the grain boundary of the FCC phases versus the BCC phase, as shown in Figure 9, the results revealed that the (AlCoCrFeNi) HEA's hardness is decreased gradually by increasing the Cu content. It is evident that the micro and macro hardness has the same trend and are nearly the same, which means high homogeneity of the new HEA. This gradual reduction in hardness can be easily described in three points: The first is incorporating more energetic binding elements, and high melting point elements like Cr in a composite increase Young's modulus and the slip resistance [62]. The second is a drop in the BCC phase with increases in the copper content FCC phase that encourages deform flexibility [27,63]. The third is attributed to the solid solution strengthening effect and the high work hardening capability for this composite.

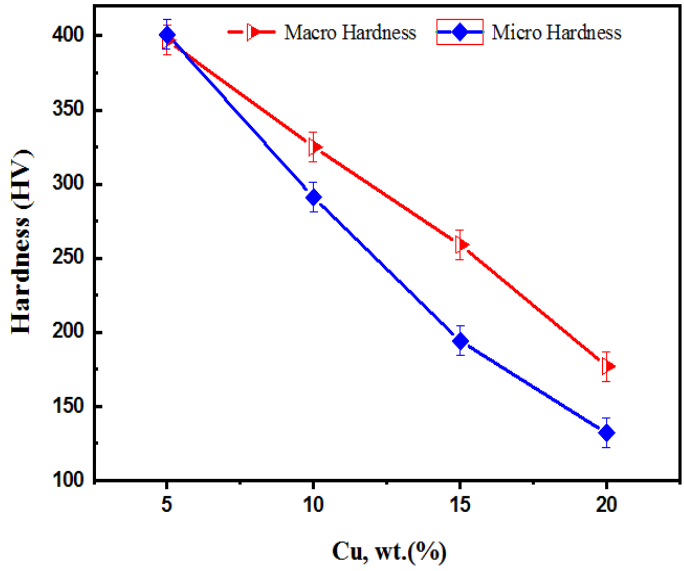

Figure 11: Vickers macro and micro hardness of HEAs fabricated samples at 950 °C.

Compression Strength

The deformation behavior of the cylindrical fabricated samples at 950 °C under a compression force in the form of stress–strain curves is shown in Figure 12. The compressive strength σ_{max} and total strain ε of all samples are listed in Table 5 to make the comparison easier. The results show that the compressive strength increases gradually by increasing the nano-copper content up to 15 wt% then decreased. Moreover, the total strain increases by increasing the amount of Cu, enhancing the alloys' flexibility and, consequently, the toughness. Increasing the strength of the fabricated HEAs samples may be due to the nano size of the precipitated copper. According to the Hall–Petch equation, there is an inversely proportional relationship between the material's strength and grain-size, where the reduction in grain size leads to an increase in material strength **[64,65]**. As shown, the AlCoCrFeNi HEAs strength has increased by increasing the percentage of the nano-copper particles that precipitated using the electroless coating process up to 15 wt% Cu then decreased. The increase in the rate of Cu nanoparticles to 20 wt% increases the agglomerations, and consequently, the grain particles that participate in dropping the strength again. On the other hand, the strain managed to grow because copper's high ductility improved its formability. The high strength and high strain of the fabricated materials mean that they have high absorption capacity (consumes a large amount of energy to deform until fracture). Additionally, increasing the strength may be due to the superb distribution and excellent adhesion among the composites' different constituents, as shown in the microstructure in **Figure 6**. The $Cu_x/(AlCoCrFeNi)_{1-x}$ HEAs' high strength is also relevant to the solid solution and the durable bonding influence among the composite metallic elements [66]. Incorporating Cr with high melting point elements in the BCC phase improves the Young's modulus and slip resistance **[67]**. On the other hand, the good elasticity and large work hardening capacity can be described by the $Cu_x/(AlCoCrFeNi)_{1-x}$ composite phase composition. According to the principal structural factor, a structure with a more slippery system leads to lower lattice friction during dislocation motion and increases the samples' elasticity **[68]**. The FCC structure has

48 slip systems against the BCC structure with 12 slip systems [69]. In this study, the composite contains two FCC phase residues and a single BCC phase. The FCC phases become dominant and hence increases the elasticity and work hardening effect. Improving the toughness of fabricated alloys by increasing the Cu's content is related to the copper's properties, where it is characterized by high toughness compared with the other used elements.

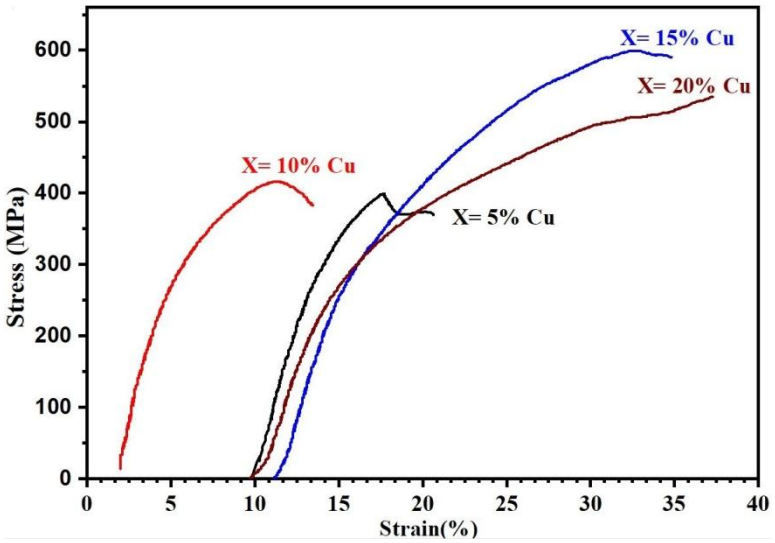

Figure 12: Compressive stress–strain curves of Cu_x/ $(AlCoCrFeNi)_{1-x}$ HEAs sintered at 950 °C.

Table 5: Compressive strength and strain of the fabricated HEAs samples.

Wt.% Cu	Compressive Stress (MPa)	strain %
5	400.03	11.53
10	416.34	20.71
15	599.53	30.82
20	535.51	31.29

Coefficient of Thermal Expansion (CTE)

The CTE of all specimens was estimated from room temperature up to 350 °C with a 3 °C/min heating rate. The effect of the Cu content and heating temperature on the CTE of the AlCoCrFeNi

for all sintered samples is shown in Figure 13. It is increased gradually by increasing the heating temperature. As the temperature increases, the kinetic energy of atoms increases, and so the CTE of the heated material does consequently. Another phenomenon from the results could be observed, which is increasing the CTE of the sintered samples with increasing Cu content. The $Cu_{0.05}$ / $(AlCoCrFeNi)_{0.95}$ recorded the lowest value of CTE 10.37 x 10^{-6} $^{o}C^{-1}$at 150 °C, whereas the $Cu_{0.2}$ / $(AlCoCrFeNi)_{0.8}$ recorded the highest one 10.95 x 10^{-6} $^{o}C^{-1}$ at the same temperature. Additionally, $Cu_{0.05}$ / $(AlCoCrFeNi)_{0.95}$ recorded the lowest value of CTE 10.71 x10^{-6} $^{o}C^{-1}$ at 350 °C, whereas the $Cu_{0.2}$ / $(AlCoCrFeNi)_{0.8}$ recorded the highest value of 11.46 x10^{-6} $^{o}C^{-1}$ at the same temperature. Increasing the CTE of the AlCoCrFeNi HEA as a result of its coating with Cu may be attributed to the high CTE of the Cu (17.6×10^{-6}) when compared to other elements, such as Cr (8.0×10^{-6}), Co (12.0×10^{-6}), Ni (13.0×10^{-6}), and Fe (12.0×10^{-6}). This fact means that the Cu_x / $(AlCoCrFeNi)_{1-x}$ can be connected with steel items or deposited as coatings on their surfaces to increase hardening and wear resistance [70,71].

So, by increasing the nano Cu percentage, the quality of Cu coating of the different elements particles increases. This leads to an increase in the overall thermal expansion of the prepared alloys. Additionally, increasing the Cu percentage from 5 up to 20 wt% increases the densification of the samples. This means that no pores are detected, which causes an increase in the dimensions of the samples by heat.

Lowering the CTE of the PM sheets makes it suitable for many thermal applications that require thermal stability of materials to keep the shape of the samples without any deformation affected by the thermal stresses during the working process. This finally leads to an increase in the lifetime of materials, which is pretty much valuable from an economic point of view [72].

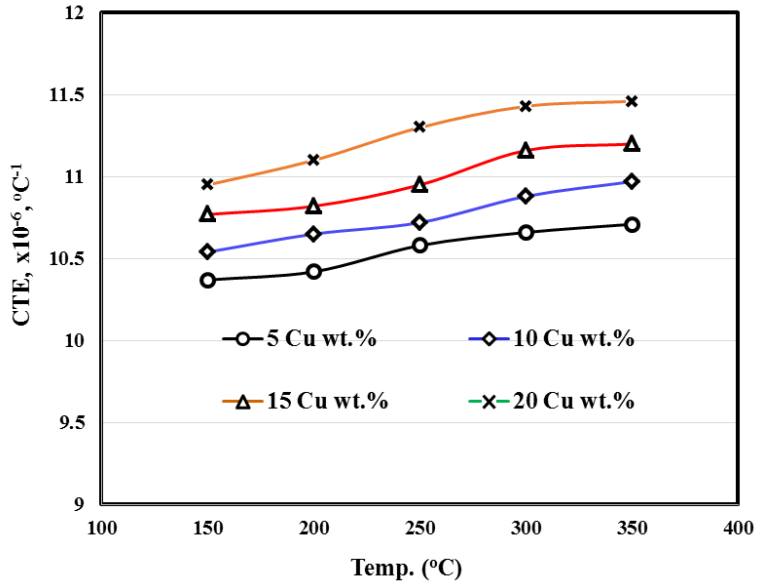

Figure 13: The coefficient of thermal expansion (CTE) of fabricated HEAs samples at different temperatures.

Conclusion

Four compositions ($Al_{19}Co_{19}Cr_{19}Fe_{19}Ni_{19}Cu_5$, $Al_{18}Co_{18}Cr_{18}Fe_{18}Ni_{18}Cu_{10}$, $Al_{17}Co_{17}Cr_{17}Fe_{17}Ni_{17}Cu_{15}$, and $Al_{16}Co_{16}Cr_{16}Fe_{16}Ni_{16}Cu_{20}$) of high entropy alloys were prepared by the powder metallurgy process at 900, 950, and 1000 °C for 90 min. Based on the results and their discussion, copper content's effect can be summarized in the following points.

- The $(AlCoCrFeNi)_{1-x}/Cu_x$ HEAs samples that sintered at 950 °C achieved the highest densification.
- The AlCoCrFeNi sample was not established with the powder metallurgy technique.
- Adding the copper element to the AlCoCrFeNi HEAs enhances its formability by the powder metallurgy technique.
- The microstructure revealed that the mechanical alloying that preceded the sintering process achieved a high

homogeneity between the different elements of the AlCoCrFeNi (HEAs), which made the elements AlCoFeNi compose the FCC matrix. An agglomeration for the Cr was established and prevented the complete forming of the HEAs.

- The mapping showed that the Cu element tends to dissolve with the FCC matrix.
- The crystallite size of the HEA powders was significantly refined as the weight percentage of Cu increased. On the other hand, the results of the lattice strain revealed that the lattice strain increased by increasing the Cu wt%.
- The crystal size of fabricated HEAs was decreased by increasing the content of the precipitated Cu, which is similar to the result of powder alloys. Additionally, the lattice strain increased by increasing the Cu content.
- The hardness of the manufactured AlCoCrFeNi HEAs decreased gradually by increasing the Cu content.
- The results showed that the compressive strength gradually increased by increasing the nano-copper content up to 15 wt% then decreased.
- According to the area under the stress–strain curves, the toughness was enhanced with the copper content.
- Precipitation of the copper in the nano size by the electroless coating process enhances the strength of the produced HEAs material according to the Hall–Petch equation.
- The CTE gradually increased by increasing the heating temperature and the content of the Cu wt%.

References

1. Yeh JW, Chen SK, Lin SJ, Gan JY, Chin TS, et al. Nanostructured high-entropy alloys with multiple principal elements: novel alloy design concepts and outcomes. Adv. Eng. Mater. 2004; 6: 299–303.
2. Cantor B, Chang I, Knight P, Vincent A. Microstructural development in equiatomic multicomponent alloys. Mater. Sci. Eng. 2004; 375: 213–218.
3. Zhang Y, Zuo TT, Tang Z, Gao MC, Dahmen KA, et al. Microstructures and properties of high-entropy alloys. Mater. Sci. 2014; 61: 1–93.

4. Ye Y, Wang Q, Lu J, Liu C, Yang Y. High-entropy alloy: challenges and prospects. Mater. Today. 2016; 19: 349–362.
5. Gorr B, Mueller F, Christ HJ, Mueller T, Chen H, et al. High temperature oxidation behavior of an equimolar refractory metal-based alloy 20Nb20Mo20Cr20Ti20Al with and without Si addition. J. Alloys Compd. 2016; 688: 468–477.
6. Gludovatz B, Hohenwarter A, Catoor D, Chang EH, George EP, et al. A fracture-resistant high-entropy alloy for cryogenic applications. Science. 2014; 345: 1153–1158.
7. Zhao J, Ji X, Shan Y, Fu Y, Yao Z. On the microstructure and erosion–corrosion resistance of AlCrFeCoNiCu high-entropy alloy via annealing treatment. Mater. Sci. Technol. 2016; 32: 1271–1275.
8. Hsu CY, Sheu TS, Yeh JW, Chen SK. Effect of iron content on wear behavior of AlCoCrFexMo0. 5Ni high-entropy alloys. Wear. 2010; 268: 653–659.
9. Amar A, Li J, Xiang S, Liu X, Zhou Y, et al. Additive manufacturing of high-strength CrMnFeCoNi-based High Entropy Alloys with TiC addition. Intermetallics. 2019; 109: 162–166.
10. Hao J, Ma Y, Wang Q, Zhang C, Li C, et al. Formation of cuboidal B2 nanoprecipitates and microstructural evolution in the body-centered-cubic Al0. 7NiCoFe1. 5Cr1. 5 high-entropy alloy. J. Alloys Compd. 2019; 780: 408–421.
11. Wei D, Li X, Schönecker S, Jiang J, Choi WM, et al. Development of strong and ductile metastable face-centered cubic single-phase high-entropy alloys. Acta Mater. 2019; 181: 318–330.
12. Kao YF, Chen TJ, Chen SK, Yeh JW. Microstructure and mechanical property of as-cast,-homogenized, and-deformed AlxCoCrFeNi ($0 \leq x \leq 2$) high-entropy alloys. J. Alloys Compd. 2009; 488: 57–64.
13. Fu X, Schuh CA, Olivetti EA. Materials selection considerations for high entropy alloys. Scripta Mater. 2017; 138: 145–150.
14. Kukshal V, Patnaik A, Bhat I. Effect of cobalt on microstructure and properties of AlCr1. 5CuFeNi2Cox high-entropy alloys. Mater. Res. Express. 2018; 5: 046514.
15. Stepanov N, Yurchenko NY, Shaysultanov D, Salishchev G, Tikhonovsky M. Effect of Al on structure and mechanical

properties of AlxNbTiVZr (x = 0, 0.5, 1, 1.5) high entropy alloys. Mater. Sci. Technol. 2015; 31: 1184–1193.
16. Wang XR, He P, Lin TS, Wang ZQ. Microstructure, thermodynamics and compressive properties of AlCrCuNixTi (x = 0, 1) high entropy alloys. Mater. Sci. Technol. 2015; 31: 1842–1849.
17. Qin G, Zhang Y, Chen R, Zheng H, Wang L, et al. Microstructures and mechanical properties of (AlCoCrFeMn) 100− xCux high-entropy alloys. Mater. Sci. Technol. 2019; 1457-1463.
18. Du W, Liu N, Peng Z, Zhou P, Xiang H, et al. Technology. The effect of Ti addition on phase selection of CoCrCu0. 5FeNi high-entropy alloys. Mater. Sci. Technol. 2018; 34: 473–479.
19. Zheng Z, Li X, Zhang C, Li J. Microstructure and corrosion behaviour of FeCoNiCuSnx high entropy alloys. Mater. Sci. Technol. 2015; 31: 1148–1152.
20. Zhang C, Zhu J, Zheng H, Li H, Liu S, et al. A review on microstructures and properties of high entropy alloys manufactured by selective laser melting. Int. J. Extreme. Manf. 2020; 2: 032003.
21. Yang Y, Luo X, Ma T, Wen L, Hu L, et al. Effect of Al on characterization and properties of AlxCoCrFeNi high entropy alloy prepared via electro-deoxidization of the metal oxides and vacuum hot pressing sintering process. J. Alloys Compd. 2021; 864: 158717.
22. Wang WR, Wang WL, Wang SC, Tsai YC, Lai CH, et al. Effects of Al addition on the microstructure and mechanical property of AlxCoCrFeNi high-entropy alloys. Intermetallics. 2012; 26: 44–51.
23. Tsai MH, Yeh JW. High-entropy alloys: a critical review. Mater. Res. Lett. 2014; 2: 107–123.
24. Xie L, Brault P, Thomann AL, Yang X, Zhang Y, et al. Molecular dynamics simulation of Al–Co–Cr–Cu–Fe–Ni high entropy alloy thin film growth. Intermetallics. 2016; 68: 78–86.
25. Santodonato LJ, Zhang Y, Feygenson M, Parish CM, Gao MC, et al. Deviation from high-entropy configurations in the atomic distributions of a multi-principal-element alloy. Nat. Commun. 2015; 6: 1–13.

26. Ogata S, Umeno Y, Kohyama M. Engineering. First-principles approaches to intrinsic strength and deformation of materials: perfect crystals, nano-structures, surfaces and interfaces. Mater. Sci. Eng. 2008; 17: 013001.
27. Tung CC, Yeh JW, Shun Tt, Chen SK, Huang YS, et al. On the elemental effect of AlCoCrCuFeNi high-entropy alloy system. Mater. Lett. 2007; 61: 1–5.
28. Dąbrowa J, Cieślak G, Stygar M, Mroczka K, Berent K, et al. Influence of Cu content on high temperature oxidation behavior of AlCoCrCuxFeNi high entropy alloys (x = 0, 0.5, 1). Intermetallics. 2017; 84: 52–61.
29. Yu Y, Shi P, Feng K, Liu J, Cheng J, et al. Effects of Ti and Cu on the microstructure evolution of AlCoCrFeNi high-entropy alloy during heat treatment. Acta Metallurgica Sinica. 2020; 1-14.
30. Jones N, Izzo R, Mignanelli P, Christofidou K, Stone H. Phase evolution in an Al0. 5CrFeCoNiCu high entropy alloy. Intermetallics. 2016; 71: 43–50.
31. Yehia HM, Daoush WM, Mouez FA, El-Sayed MH, El-Nikhaily AE. Microstructure, Hardness, Wear, and Magnetic Properties of (Tantalum, Niobium) Carbide- Nickel–Sintered Composites Fabricated from Blended and Coated Particles. Mater. Perform. Charact. 2020; 4: 543–555.
32. Yehia HM, Allam S. Allam Hot Pressing of Al‐10 wt% Cu‐10 wt% Ni/x (Al_2O_3–Ag) Nanocomposites at Different Heating Temperatures. Metal Mater. Int. 2007; 107: 2411-2502.
33. El-Tantawy A, El Kady OA, Yehia HM, Ghayad IM. Effect of Nano ZrO_2 Additions on the Mechanical Properties of Ti-12Mo Composite by Powder Metallurgy Route. Key Eng. Mater. 2020; 835: 367–373
34. Eißmann N, Klöden B, Weißgärber T, Kieback B. High-entropy alloy CoCrFeMnNi produced by powder metallurgy. Powder Metall. 2017; 60: 184–197.
35. Yehia HM, Abu-Oqail A, Elmaghraby MA, Elkady OA. Microstructure, hardness, and tribology properties of the (Cu/MoS_2)/graphene nanocomposite via the electroless deposition and powder metallurgy technique. J. Compos. Mater. 2020; 1–12.

36. El-Kady O, Yehia HM, Nouh F, Materials H. Preparation and characterization of Cu/(WC-TiC-Co)/graphene nano-composites as a suitable material for heat sink by powder metallurgy method. Int. J. Refract. Met. Hard Mater. 2019; 79: 108–114.
37. Testing ASF, Powders MCBOM, Products MP. Standard Test Methods for Density of Compacted or Sintered Powder Metallurgy (PM) Products Using Archimedes' Principle. West Conshohocken: ASTM. 2014; 7.
38. Scherrer P. Determination of the size and internal structure of colloidal particles using X-rays. Nachr. Ges. Wiss. Göttingen. 1918; 2: 98–100.
39. Danilchenko S, Kukharenko O, Moseke C, Protsenko IY, Sukhodub L, et al. Determination of the bone mineral crystallite size and lattice strain from diffraction line broadening. J. Exper. Ind. Crystallogr. 2002; 37: 1234–1240.
40. ASTM standard E384. West Conshohocken: ASTM International. 2011; 19428-2959. Avaialble Online at: https://www.astm.org/Standards/E384
41. Jianhong L, Yun J, Haiping L, Jiguo T, Shu-qiang J. Influence of EDTA/THPED Dual-Ligand on Copper Electroless Deposition. Int. J. Electrochem. 2018, 13, 6015–6026.
42. Yuan Y, Gan X, Lai Y, Zhao Q, Zhou K. Microstructure and properties of graphite/copper composites fabricated with Cu-Ni double-layer coated graphite powders. Comp. Interf. 2020; 27: 449–463.
43. Yusoff M, Hussain Z. Manufacturing. Effect of sintering parameters on microstructure and properties of mechanically alloyed copper-tungsten carbide composite. Int. J. Mater, Mech. Manuf. 2013; 1: 283–286.
44. An Z, Jia H, Wu Y, Rack PD, Patchen AD, et al. Solid-solution CrCoCuFeNi high-entropy alloy thin films synthesized by sputter deposition. Mater. Res. Lett. 2015; 3: 203–209.
45. Shivam V, Basu J, Pandey VK, Shadangi Y, Mukhopadhyay N. Alloying behaviour, thermal stability and phase evolution in quinary AlCoCrFeNi high entropy alloy. Adv. Powder Technol. 2018; 29: 2221–2230.

46. Suryanarayana C, Ivanov E, Boldyrev VA. The science and technology of mechanical alloying. Mater. Sci. Eng. 2001; 304: 151–158.
47. Shang C, Axinte E, Sun J, Li X, Li P, et al. CoCrFeNi (W1−xMox) high-entropy alloy coatings with excellent mechanical properties and corrosion resistance prepared by mechanical alloying and hot pressing sintering. Mater. Des. 2017; 117: 193–202.
48. Bonache V, Salvador M, Fernández A, Borrell A, Materials H. Fabrication of full density near-nanostructured cemented carbides by combination of VC/Cr3C2 addition and consolidation by SPS and HIP technologies. Int. J. Refract. Met. Hard Mater. 2011; 29: 202–208.
49. Fang S, Chen W, Fu Z. Microstructure and mechanical properties of twinned Al0. 5CrFeNiCo0. 3C0. 2 high entropy alloy processed by mechanical alloying and spark plasma sintering. Mater. Des. 2014; 54: 973–979.
50. Yeh JW, Lin SJ, Chin TS, Gan JY, Chen SK, et al. Formation of simple crystal structures in Cu-Co-Ni-Cr-Al-Fe-Ti-V alloys with multiprincipal metallic elements. Metall. Mater. Trans. 2004; 35: 2533–2536.
51. Ibrahim A, Abdallah M, Mostafa S, Hegazy AA. An experimental investigation on the W–Cu composites. Mater. Des.2009; 30: 1398–1403.
52. Huang PK, Yeh JW, Shun TT, Chen SK. Multi-principal-element alloys with improved oxidation and wear resistance for thermal spray coating. Adv. Eng. Mater. 2004; 6: 74–78.
53. Ogura M, Fukushima T, Zeller R, Dederichs PH. Structure of the high-entropy alloy AlxCrFeCoNi: fcc versus bcc. J. Alloys Compd. 2017; 715: 454–459.
54. Zhu JM, Meng JL, Liang JL. Microstructure and mechanical properties of multi-principal component AlCoCrFeNiCu x alloy. Rare Met. 2016; 35: 385–389.
55. Kim DG, Jo YH, Park JM, Choi WM, Kim HS, et al. Effects of annealing temperature on microstructures and tensile properties of a single FCC phase CoCuMnNi high-entropy alloy. J. Alloys Compd. 2020; 812: 152111.
56. Sriharitha R, Murty B, Kottada RS. Phase formation in mechanically alloyed AlxCoCrCuFeNi (x = 0.45, 1, 2.5, 5 mol) high entropy alloys. Intermetallics. 2013; 32: 119–126.

57. Chen YL, Hu YH, Hsieh CA, Yeh JW, Chen SK. Competition between elements during mechanical alloying in an octonary multi-principal-element alloy system. J. Alloys Compd. 2009; 481: 768–775.
58. Liu XT, Lei WB, Li J, Ma Y, Wang WM, e t al. Laser cladding of high-entropy alloy on H13 steel. Rare Met. 2014; 33: 727–730.
59. Porter D, Easterling E, Sherif M. Crystal Interfaces and Microstructure. Phase Transformations in Metals and Alloys. New York: CRC Press. 1992.
60. Takeuchi A, Inoue A. Classification of bulk metallic glasses by atomic size difference, heat of mixing and period of constituent elements and its application to characterization of the main alloying element. Metall. Mater. Trans. 2005; 46: 2817–2829.
61. Gwalani B, Choudhuri D, Soni V, Ren Y, Styles M, et al. Cu assisted stabilization and nucleation of L12 precipitates in Al0. 3CuFeCrNi2 fcc-based high entropy alloy. Acta Mater. 2017; 129: 170–182.
62. Wu JM, Lin SJ, Yeh JW, Chen SK, Huang YS, et al. Adhesive wear behavior of AlxCoCrCuFeNi high-entropy alloys as a function of aluminum content. Wear. 2006; 261: 513–519.
63. Reed-Hill RE, Abbaschian R. Physical Metallurgy Principles, 3rd ed. Boston: PWS-KENT Publishing Company. 1994; 140–146.
64. Qiu XW. Microstructure and properties of AlCrFeNiCoCu high entropy alloy prepared by powder metallurgy. J. Alloys Compd. 2013; 555: 246–249.
65. Nyanor P, El-Kady O, Yehia HM, Hamada AS, Hassan MA. Effect of Bimodal-Sized Hybrid TiC–CNT Reinforcement on the Mechanical Properties and Coefficient of Thermal Expansion of Aluminium Matrix Composites. Met. Mater. Int. 2020; 27: 753–766.
66. Harwood J. Strengthening Mechanisms in Solids, Metals Park: ASM Seminar. 1960.
67. Wen L, Kou H, Li J, Chang H, Xue X, et al. Effect of aging temperature on microstructure and properties of AlCoCrCuFeNi high-entropy alloy. Intermetallics. 2009; 17: 266–269.

68. Dieter GE, Bacon DJ. Mechanical Metallurgy. New York: McGraw-hill. 1986; 3.
69. Zhang K, Fu Z, Zhang J, Shi J, Wang W, et al. Annealing on the structure and properties evolution of the CoCrFeNiCuAl high-entropy alloy. J. Alloys Compd. 2010; 502: 295–299.
70. Barakat WS, Elkady O, Abu-Oqail A, Yehya HM, EL-Nikhaily A. Effect of Al_2O_3 Coated Cu Nanoparticles on Properties of Al / Al_2O_3 Composites. J. Petroleum Min. Eng. 2020; 22.
71. Nadutov V, Makarenko SY, Svystunov YO. Effect of Al content on magnetic properties and thermal expansion of as-cast high-entropy alloys AlxFeCoNiCuCr. Металлофизика Новейшие Технологии. 2015; 37: 987–1000.
72. Yehia HM, Elkady OA, Reda Y, Ashraf KM. Electrochemical surface modification of aluminum sheets prepared by powder metallurgy and casting techniques for printed circuit applications. Trans. Indian Inst. Met. 2019; 72: 85–92.